J Nanopart Res (2018) 20: 183
https://doi.org/10.1007/s11051-018-4284-5

RESEARCH PAPER

Electrochemical performance of interspace-expanded molybdenum disulfide few-layer

Yibing Xie · Panqin Sun

Received: 1 December 2017 / Accepted: 27 June 2018 / Published online: 7 July 2018

Abstract Interspace-expanded molybdenum disulfide (IE-MoS_2) has been designed as a supercapacitor electrode material to improve the cycling stability. IE-MoS_2 was formed through the ultrasound exfoliation of the interspace-compacted molybdenum disulfide (IC-MoS_2), which was initially prepared through hydrothermal synthesis using Na_2MoO_4 as molybdenum source and CH_4N_2S as sulfur source. As-formed IE-MoS_2 shows a few-layer structure with approximate 8–16 monolayer packing and monolayer distance of 0.83 nm. The MoS_2 few-layer distance increased from 12 nm of IC-MoS_2 to 20 nm for IE-MoS_2. The specific capacitance was determined to be 108 F g^{-1} for IC-MoS_2 to 192 F g^{-1} for IE-MoS_2 at 0.5 A g^{-1}. The improved specific capacitance was ascribed to more active sulfur atom exposed at the edges of IE-MoS_2 few-layer to conduct the promoted proton attachment reaction. IE-MoS_2 showed the capacity retention of 42% when the current density increased from 0.5 to 10 A g^{-1}, presenting the high-rate capability. IE-MoS_2 achieved the capacity retention of 116% at 10 A g^{-1} after 5000 charge-discharge cycles, which was ascribed to the electro-activation of the few-layer expanded MoS_2 in proton acid electrolyte solution. IE-MoS_2 exhibited the obviously improved cycling stability in comparison with IC-MoS_2. All solid-state IE-MoS_2 supercapacitor based on two symmetric IE-MoS_2 electrodes and H_2SO_4-PVA gel electrolyte exhibited the energy density of 18.75 Wh kg^{-1} and power density of 375 W kg^{-1} at 0.5 A g^{-1} and high voltage window of 1.5 V. IE-MoS_2 supercapacitor also exhibited the improved capacity retention of 110% after 1000 charge-discharge cycles. Such well-designed IE-MoS_2 few-layer with highly improved cycling stability performance presented the promising energy storage application.

Keywords Molybdenum disulfide · Ultrasound exfoliation · Cycling stability · Electrode material · Supercapacitor

Y. Xie (✉) · P. Sun
School of Chemistry and Chemical Engineering, Southeast University, Nanjing 211189, China
e-mail: ybxie@seu.edu.cn

Introduction

In recent decades, lithium ion batteries and supercapacitors have shown the good electrochemical performance and broad application prospect owing to high-energy density, power density cycling performance (Park et al. 2014; Xie 2017). Generally, there are three kinds of supercapacitor electrode materials such as carbon materials, conductive polymers, and transition metal oxides or sulfides (Xie and Wang 2018; Zhou and Xie 2017). Carbon materials with high surface area are widely used in electrical double-layer capacitors. Although carbon materials possess good cycling stability, low specific capacitance is a fatal flaw (Zhao and Xie 2017). High specific capacitance and poor cycling stability are the features of conductive polymers (Xiao et al. 2017; Xie and Sha 2018). Comparatively, layer-structured two-dimensional transition metal oxides or

sulfides have considerable theoretical capacity and electrochemical properties because of its inherently layered structure (Fei et al. 2014; Xie and Tian 2017). Therefore, the transition metal oxides or sulfides were widely regarded as the promising electrode materials of pseudocapacitors owing to the low-cost, environmentally friendly feature and high theoretical specific capacitance (Lu and Xie 2017; Lu et al. 2018; Xie and Gao 2017).

Molybdenum disulfide as a typical layered transitionmental dichalcogenides has sandwich-like structure, exhibiting unique physical and chemical peculiarities (Liu et al. 2012; Xiong et al. 2015). MoS_2 involves Mo–S strong covalent bonds in single molecular layer and weak van der Waals force between the interlayers, which permits the intercalation of electrolyte ions (Bissett et al. 2015). Layered molybdenum disulfide (MoS_2) electrode material shows the following multiple advantages (Yu et al. 2017). The high surface area ensures large electrode-electrolyte contact area and electrochemical actives sites. The permeable thin shells can shorten the ion diffusion length and electron transportation route. The layered structure can effectively release the stress-induced structural variation during long-time charge-discharge process. MoS_2 has high theoretical specific capacitance of 900~1200 mAh g^{-1} (Du et al. 2010), presenting much higher value than 371 mAh g^{-1} of graphene (Lee et al. 2012). Therefore, MoS_2 presents an application prospect in the field of energy storage. The preparation methods of MoS_2 include the reduction of molybdate salt and molybdenum vulcanization. MoS_2 nanofibers or nanoflowers were reported to be prepared through hydrothermal synthesis method using molybdate salt as molybdenum source and thiourea as sulfur source in acidic medium (Hu et al. 2014; Nagaraju et al. 2007). Interspace-compacted MoS_2 (IC-MoS_2) usually showed the small interlayer distance of about 6.15 Å and the low conductivity of 3.3×10^{-7} S cm^{-1} (Wang et al. 2015), which lowered the accessible surface areas and cycling stability to a certain extent. Therefore, such an IC-MoS_2 electrode material usually exhibited low specific capacitance and capacity retention during long-time charge-discharge process (Wu et al. 2016). It was reported that MoS_2 nanosheet prepared by in situ hydrothermal growth technique revealed the specific capacitance of 146.15 F g^{-1} and the capacity retention of only 17% after 1000 charge-discharge cycles (Patel et al. 2016). One of the unique properties of 2D-layered materials was capable to intercalate guest species into the van der Waals gaps (Yoo et al. 2016). Therefore, many efforts were conducted to improve the specific capacitance and cycling performance by expanding interlayer distance of MoS_2 (Tang et al. 2015). The ion intercalation or ultrasound exfoliation become reasonable methods to enlarge the interlayer spaces (Matte et al. 2010). Comparatively, ultrasound-assisted stripping method seems more effective to peel off the layered-structured MoS_2 into few-layer (Wang et al. 2016). The reaction solvent is mainly related to its surface tension of MoS_2, which could lead to the smaller exfoliation energy and the better dispersion effect (Cunningham et al. 2012). N,N-dimethylformamide (DMF) and N-methyl-2-pyrrolidone (NMP) were used for the liquid-phase ultrasound exfoliation to obtain MoS_2 few-layer (Ghasemi and Mohajerzadeh 2016; Wang et al. 2016). Comparatively, DMF solvent could act as the reducing agent and the oxygen donor, which could expand interlayer spaces and meanwhile improve intrinsic conductivity of MoS_2 (Liu et al. 2016). In this study, interspace-expanded MoS_2 was prepared by peeling off interspace-compacted MoS_2 using liquid-phase ultrasound exfoliation method. The electrochemical performance of interspace-expanded MoS_2 few-layer was fully investigated to act as supercapacitor electrode material.

Experimental

Materials

Sodium molybdate dihydrate ($Na_2MoO_4{\cdot}2H_2O$); thiourea (CH_4N_2S); poly (vinylidene fluoride) (PVDF); N-methyl-pyrrolidone (NMP); N,N-dimethylformamide (DMF); sulfuric acid (H_2SO_4); lithium sulfate (Li_2SO_4); and sodium sulfate ($Na2SO_4$) were purchased from Sinopharm chemical reagent Co., Ltd. Deionized water was used throughout all experiments.

Preparation of IC-MoS_2 and IE-MoS_2

Figure 1 shows the schematic illustrating the preparation of interspace-expanded molybdenum disulfide (IE-MoS_2) few-layer. Firstly, IC-MoS_2 was prepared through hydrothermal synthesis method using $Na_2MoO_4{\cdot}2H_2O$ as molybdenum source and CH_4N_2S as sulfur source. In detail, 1.21 g $Na_2MoO_4{\cdot}2H_2O$ and 1.56 g CH_4N_2S were dissolved in 30-ml deionized water

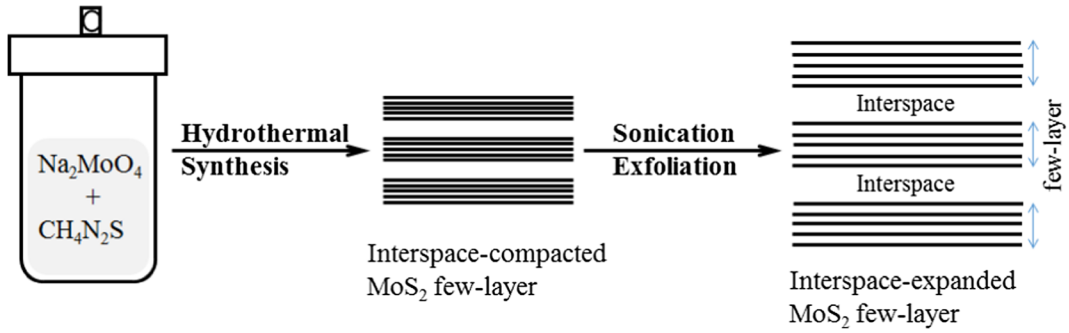

Fig. 1 Schematic illustrating the preparation of the interspace-expanded MoS_2 few-layer through hydrothermal synthesis and ultrasound exfoliation process

and then added into 50-ml Teflon-lined stainless steel autoclave, reacting in 220 °C for 24 h. The product was washed with ethanol and deionized water for several times and dried at 60 °C in a vacuum. Finally, black product was obtained and denoted as IC-MoS_2. Secondly, IE-MoS_2 was prepared through liquid-phase ultrasound exfoliation process in DMF solvent (Wang et al. 2016). In a typical process, 1.0 g IC-MoS_2 was added into 100 ml of DMF followed by sonication treatment for 2 h. The suspension was centrifuged at 2000 rpm min^{-1} for 30 min and the sediment was discarded to remove unexfoliated or thick MoS_2 flakes. The suspension was dried at 60 °C until the liquid is completely volatilized. The obtained gray product was denoted as IE-MoS_2.

Figure 2 shows photographs of electroactive electrodes of IC-MoS_2 and IE-MoS_2 few-layer supporting on carbon paper and all-solid-state IE-MoS_2 supercapacitor. The IC-MoS_2 and IE-MoS_2 electrodes were prepared by mixing 80 wt% electroactive materials, 10 wt% acetylene black, and 10 wt% polyvinylidene fluoride (PVDF) in NMP solvent, and then coating on carbon paper (1 cm × 5 cm) in vacuum at 80 °C. The loading mass is approximately 0.5 mg cm^{-2}. All-solid-state IE-MoS_2 supercapacitor was constructed using two symmetric IE-MoS_2 electrodes and H_2SO_4-PVA gel electrolyte.

Characterization and measurement

The electrochemical measurement was conducted using CHI 760 electrochemical workstation with a standard three-electrode system. A Pt plate and the saturated calomel electrode (SCE) were used as the counter and the reference electrode, respectively. The reaction electrolyte solution was 1 M H_2SO_4, 1 M Li_2SO_4, and 1 M Na_2SO_4 aqueous solution. Cyclic voltammetry (CV) measurements were conducted at a potential range of − 0.2~0.6 V vs. SCE at scan rates from 5 to 200 mV s^{-1}. Galvanostatic charge and discharge (GCD) measurements was conducted at a potential range of − 0.2~0.6 V vs. SCE at a current density of 0.5, 1, 2, 3, 5, and 10 A g^{-1}, respectively. Electrochemical impedance spectroscopy (EIS) was conducted in the frequency range of 10^{-2}~10^{5} Hz. Cycling stability measurements were conducted using LAND CT2001A battery testing system. The specific capacitance (C), energy density (E), and power density (P) are calculated using the following equations:

$$C = \frac{Q}{\Delta V \times m} = \frac{I \times t}{\Delta V \times m} \quad (1)$$

$$P = \frac{I \times \Delta V}{2m} \quad (2)$$

$$E = \frac{C \times (\Delta V)^2}{2} \quad (3)$$

where C is the specific capacitance, I is the charge-discharge current, t is the time of discharge, ΔV is the voltage difference between the upper and lower potential limits, and m is the mass of active materials.

The morphology and microstructure of electrode materials were characterized by means of scan electron microscopy (SEM, Zeiss Ultra Plus); transmission electron microscopy (TEM, JEM-2100); and energy-dispersive x-ray (EDX, Zeiss Ultra Plus). Raman spectroscopy was performed on a Raman spectrometer (Raman, Renishaw microRaman spectroscopy) using a He–Ne that emitted the samples at 532-nm excitation with

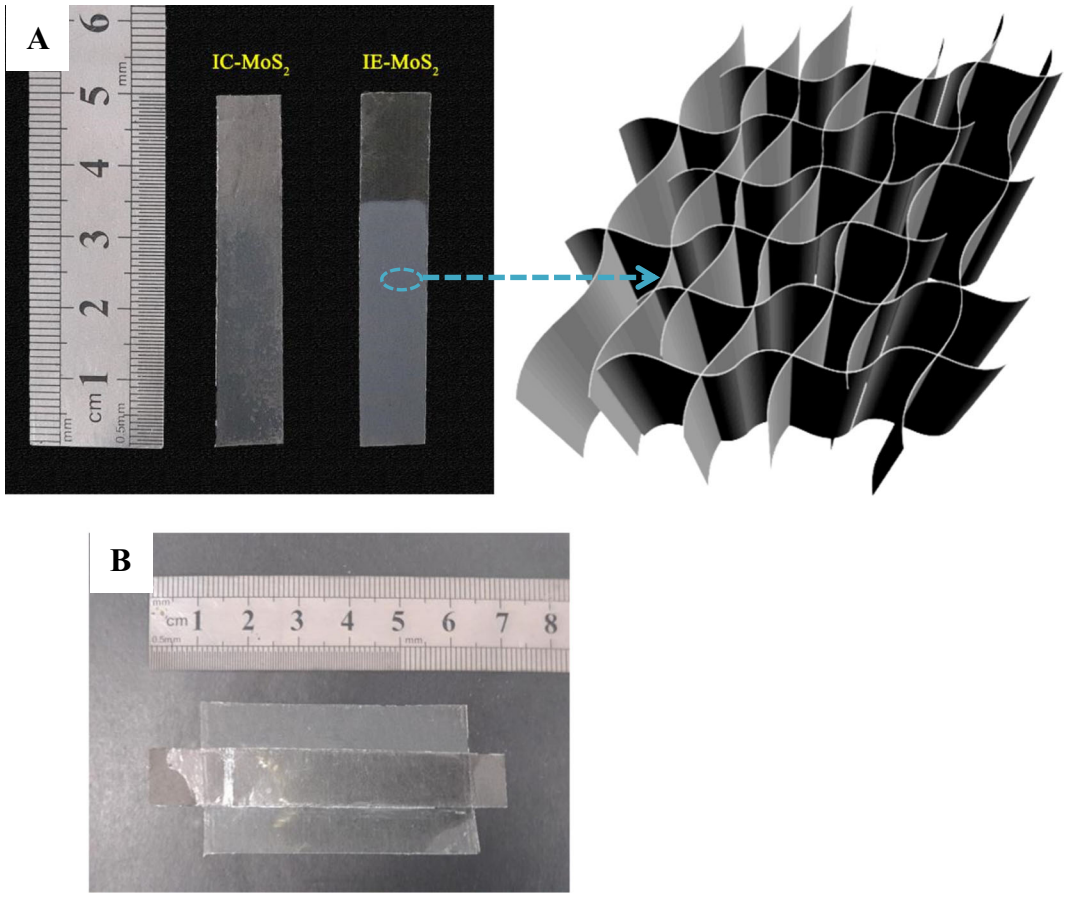

Fig. 2 Photographs of **a** electroactive electrodes of IC-MoS_2 and IE-MoS_2 few-layer supporting on carbon paper and **b** all-solid-state IE-MoS_2 supercapacitor

wave between 0 and 2000 cm^{-1}. X-ray diffraction (XRD, Bruker D8 Advance) were obtained with the use of Cu-Kα radiation source ($\lambda = 1.54178$ Å) operating at 40 kV and 40 Å.

Results and discussion

Morphological characterization

Figure 3a–f shows the SEM images of IC-MoS_2 and IE-MoS_2. As-formed IC-MoS_2 and IE-MoS_2 reveal the whole spherical particle morphology (Fig. 3a, d). IE-MoS2 shows rougher surface than IC-MoS2. Both IC-MoS_2 and IE-MoS_2 have the nanoflower morphology and the lamellar microstructure (Fig. 3b, e). The interspace distance is 150–200 nm for IC-MoS_2 few-layer and 200–250 nm for IE-MoS_2 (Fig. 3c, f). IE-MoS_2 few-layer keeps larger interspace distance than IC-MoS_2. The lamellar structure usually contributes to much larger surface area than the conventional block structure, which could enhance the effective contact area (Wang et al. 2016). The expanded interspace with the improved accessible surface area could facilitate the ion diffusion in electrochemical reaction process. Figure 3g, h show the TEM images of IC-MoS_2 and IE-MoS_2. Generally, the IC-MoS_2 has d-spacing (interlayer distance or layer-layer distance) of about 0.62–0.63 nm for (002) crystal plane (Xiong et al. 2015; Zhang et al. 2017a). Comparatively, IE-MoS_2 few-layer has the d-spacing (interlayer distance) of 0.83 nm for (002) crystal plane, which is obviously larger than IC-MoS_2 (Wang et al. 2017a; Xiao et al. 2017). Therefore, DMF-assisted exfoliation ultrasound could effectively expand the interspace distance and interlayer distance of IC-MoS_2. The hydrothermal reaction of Na_2MoO_4·and $CS(NH_2)_2$ could produce the layer-structured IC-MoS_2. In ultrasound exfoliation process, DMF molecule could enter into the van der Waals

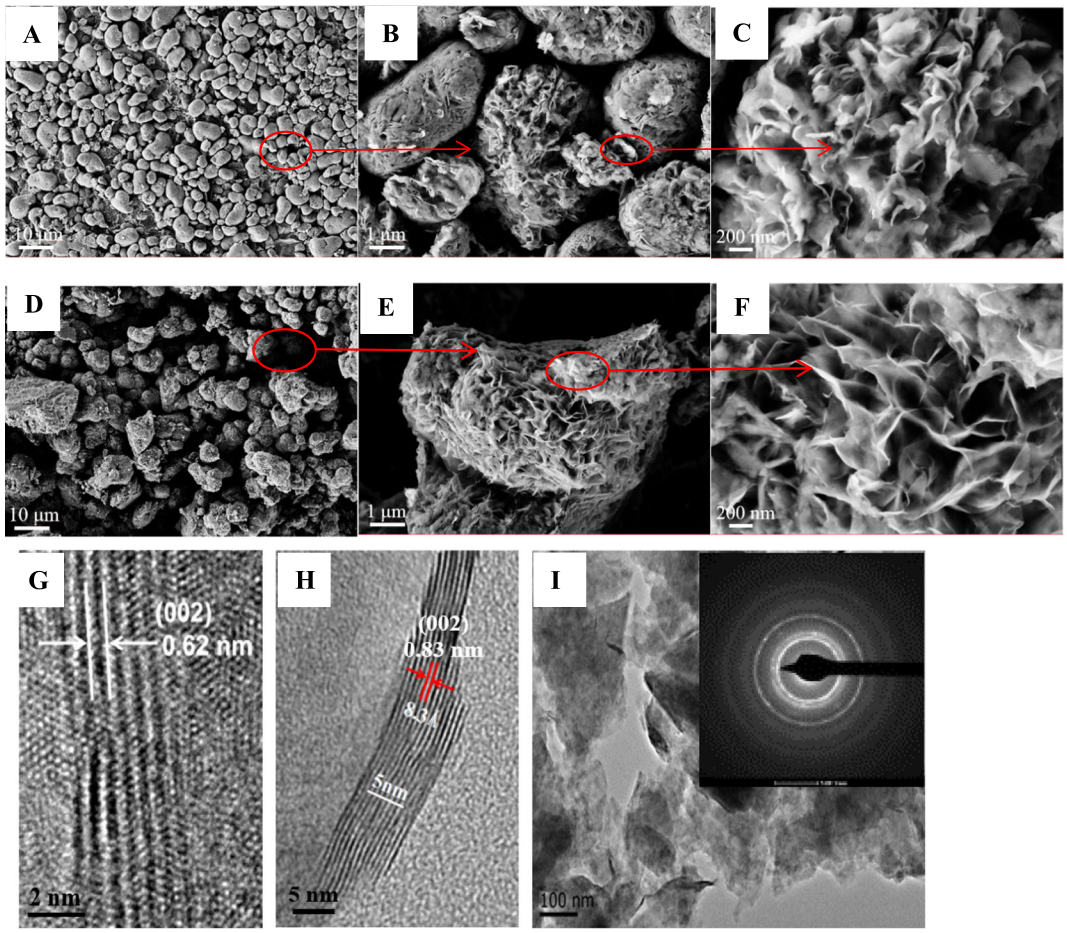

Fig. 3 SEM images of **a**–**c** IC-MoS_2 and **d**–**f** IE-MoS_2. TEM images of **g** IC-MoS_2 and **h**, **i** IE-MoS_2

gaps of MoS_2 interlayers, resulting in interlayer-expanded IE-MoS_2. Meanwhile, the sonication exfoliation also could enlarge the distance of MoS_2 few-layer, resulting in the interspace-expanded IE-MoS_2. So, organic molecule insertion and sonication exfoliation method could well expand both interlayer distance and interspace distance of MoS_2. Figure 3h shows TEM and SAED pattern of IE-MoS_2. IE-MoS_2 reveals the few-layered structure. The presence of distinct diffraction rings indicate that IE-MoS_2 presents the well-defined crystal structure.

Structural analysis

Figure 4a shows the Raman spectra of IC-MoS_2 and IE-MoS_2. Both IC-MoS_2 and IE-MoS_2 exhibited the strong characteristic Raman peaks at the wavenumber of 376 cm^{-1} (or 378 cm^{-1}) and 402 cm^{-1} (or 404 cm^{-1}), which were assigned to $E_{2g}{}^1$ and A_{1g} vibration modes, respectively (Hu et al. 2014; Jeong et al. 2015). The $E_{2g}{}^1$ peak at 376 cm^{-1} (or 378 cm^{-1}) was ascribed to the in-plane bending vibration of Mo and S atoms. The A_{1g} peak at 402 cm^{-1} (or 404 cm^{-1}) was ascribed to the out of plane bending vibration of the S atom (Xiong et al. 2015). The $E_{2g}{}^1$ and A_{1g} peaks shifted from 378 and 404 cm^{-1} for the IC-MoS_2 to 376 and 402 cm^{-1} for the IE-MoS_2, presenting the red-shift effect. The IE-MoS_2 with the increased interlayer distance has the lowered Van der Waals force, causing the red-shift of A_{1g} and $E_{2g}{}^1$ Raman peaks of MoS_2 (Liu et al. 2015). So, Raman spectrum analysis result is well consistent with the TEM characterization result that the d-spacing increases from 0.63 nm for IC-MoS_2 to 0.83 nm for IE-MoS_2.

In general, layer-structured MoS_2 has three crystal forms of 1T, 2H, and 3R. The monolayer MoS_2 usually shows 1T crystal phase (Acerce et al. 2015). Few-layer and multilayer MoS_2 usually shows 2H crystal phase, which is the most stable crystal structure (Wang et al.

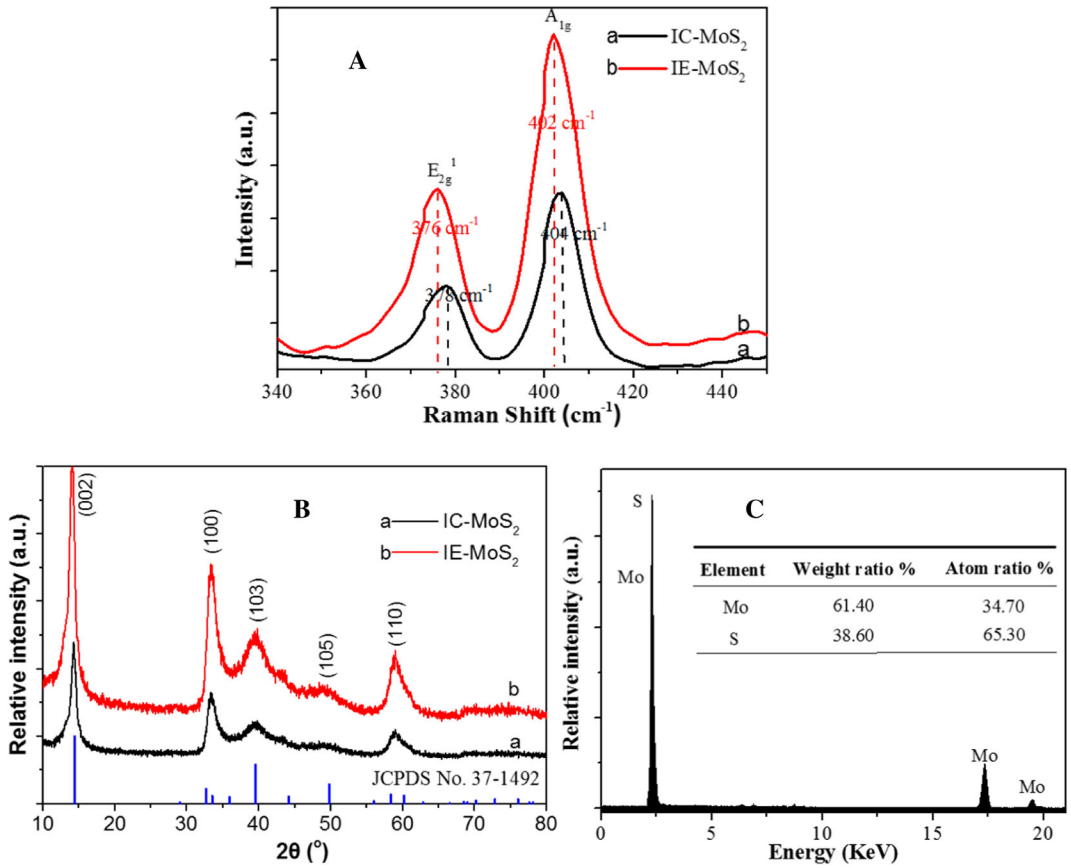

Fig. 4 **a** Raman spectra and **b** XRD patterns of IC-MoS_2 and IE-MoS_2. **c** EDX spectrum of IE-MoS_2

2017b). It has been widely reported that IC-MoS_2 synthesized by hydrothermal reaction of Na_2MoO_4 and $CS(NH2)_2$ is multilayer-structured MoS_2 with 2H crystal phase (Lu et al. 2015). Herein, IE-MoS_2 is formed by DMF-assisted ultrasound exfoliation of multilayer-structured MoS_2. The x-ray diffraction characterization is carried out to determine the crystal phase of IE-MoS_2. Figure 4b shows the XRD patterns of IC-MoS_2 and IE-MoS_2. IE-MoS_2 demonstrates the characteristic diffraction peaks at $2\theta = 14.1°$, 33.7°, 39.5°, 49.4°, and 58.9°, which are corresponding to the crystal planes of (002), (100), (103), (105), and (110), respectively. Similar characteristic diffraction peaks of IC-MoS_2 are observed except for the 2θ diffraction angle at 14.3° for crystal planes of (002). The characteristic diffraction peaks of IC-MoS_2 and IE-MoS_2 are consistent with the standard diffraction peaks of MoS_2 with 2H crystal phase (JCPDS No. 37-1492) (Liu et al. 2012). The impurity crystal phase was not observed, indicating the high-yield formation of 2H phase of MoS_2 in the hydrothermal synthesis process. So, IE-MoS_2 few-layer exhibit 2H crystal phase form. The (002) crystal plane peak shift to the small diffraction angle indicates the increase of (002) interplanar spacing, leading to the interlayer expansion of IE-MoS_2. This result agrees with TEM analysis result that the d-spacing increases from 0.63 nm for IC-MoS_2 to 0.83 nm for IE-MoS_2. IE-MoS_2 still keeps few-layer structure rather than monolayer structure.

Figure 4c shows the EDX spectrum of IE-MoS_2. The energy-dispersive peaks at about 2.3, 17.3, and 19.5 kev are ascribed to Mo element. The energy-dispersive peak at about 2.3 keV is also ascribed to S element. The inset table lists the calculated weight ratio and atom ratio of Mo and S elements of MoS_2. The atom ratio of S/Mo was approximately close to be 2, which was in accordance with the stoichiometric ratio of MoS_2. No other element could be found in the EDX spectra.

Electrochemical performance

The electrochemical properties of IC-MoS_2 and IE-MoS_2 investigated through CV and GCD measurements in 1 M H_2SO_4 solution. Figure 5a, b shows the CV curves at a scan rate of 5 mV s^{-1} and GCD curves at 0.5 A g^{-1} of IC-MoS_2 and IE-MoS_2. The CV curves of IE-MoS_2 at a low scan rate of 5 mV s^{-1} exhibit an obvious pair of redox peaks in 1 M H_2SO_4 electrolyte solution, which is corresponding to anodic peak at 0.52 V and cathodic peak at 0.14 V. The redox peaks of MoS_2 are associated with proton insertion/desertion into MoS_2 interlayer. The redox process occurred on IE-MoS_2 is related with the active atoms located at the edge of the exposed few-layer (Mahmood et al. 2016; Soon and Loh 2007; Temel et al. 2010). Sulfur atoms, exposed at the edges of IE-MoS_2 few-layer, can reversibly attach protons in the acidic electrolyte, thus changing the oxidation state of the neighboring Mo atoms from 4^+ to $(4-\delta)^+$ according to the proton attachment reaction of $MoS_2 + H^+ + e^- \rightleftharpoons$ MoS–SH (Koroteev et al. 2016). The reversible redox process causes the deviation of CV curves from normal rectangular shape, suggesting the typical pseudocapacitive behavior (Zhang et al. 2015). Comparatively, the redox peaks of IC-MoS_2 became insignificant. Generally, the IC-MoS_2 presents the compacted few-layer structure with smaller monolayer distance than IE-MoS_2. Less active sulfur atoms mostly cause a lower electroactivity to conduct the proton attachment reaction. Accordingly, the weakened redox process of IC-MoS_2 leads to the reduced current response as well. According to the GCD measurements and equation 1, the specific capacitance of IC-MoS_2 and IE-MoS_2 was 108 and 192 F g^{-1} at 0.5 A g^{-1}, respectively. The corresponding IR drop was 20.3 and 27.7 mV, respectively. IE-MoS_2 shows the increased capacitance and the decreased internal resistance. Figure 5c shows the capacitance curves in dependence on different current densities. The capacitance retention was 22 and 42% when the current density increased

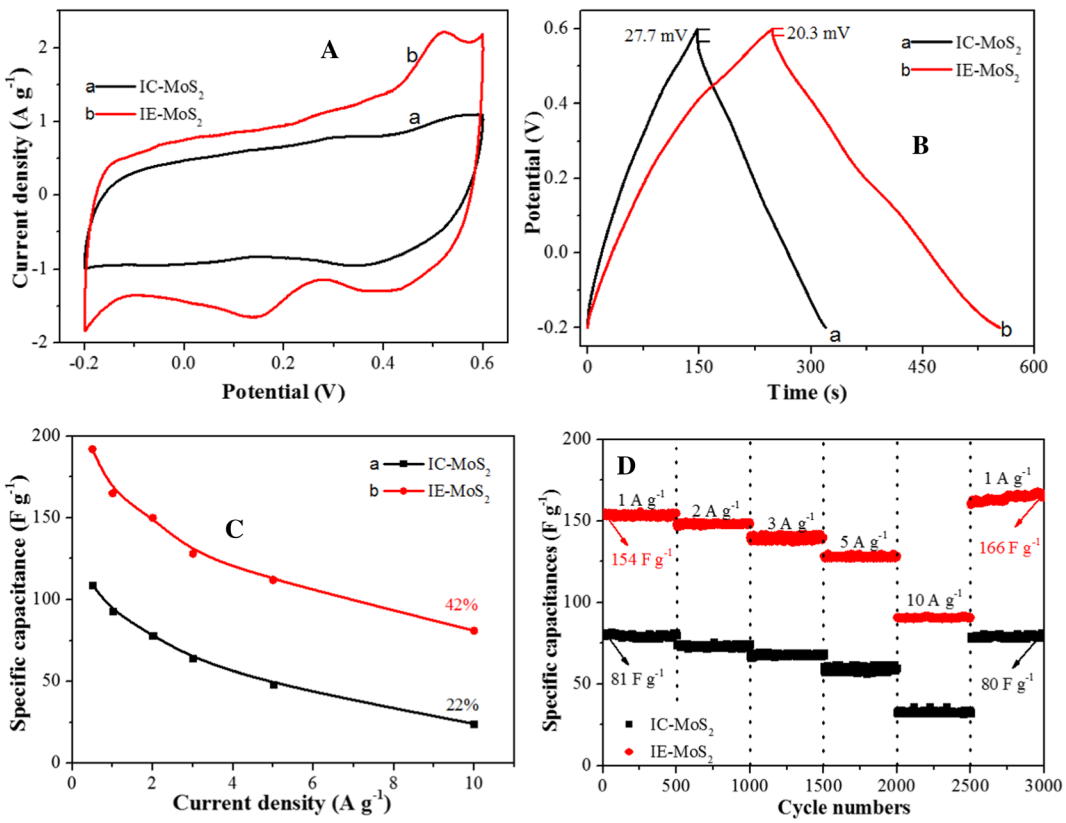

Fig. 5 **a** CV curves of IC-MoS_2 and IE-MoS_2 at a scan rate of 5 mV s^{-1} in 1 M H_2SO_4 electrolyte solution. **b** GCD curves of IC-MoS_2 and IE-MoS_2 at 0.5 A g^{-1} in 1 M H_2SO_4 solution. **c** Specific capacitance of IC-MoS_2 and IE-MoS_2 at different current densities. **d** Rate capability performance of IC-MoS_2 and IE-MoS_2 at different current densities during cycling charge-discharge process

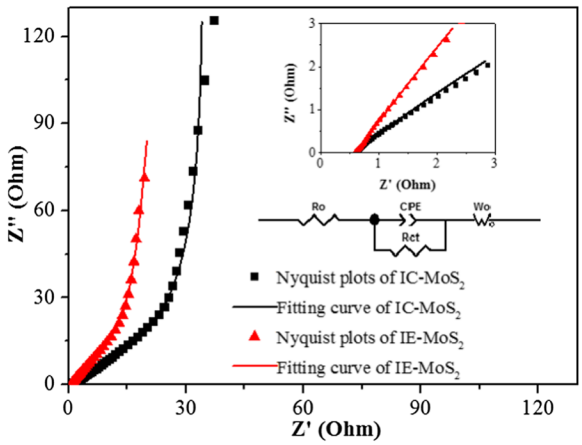

Fig. 6 EIS Nyquist plots of IC-MoS_2 and IE-MoS_2 in 1 M H_2SO_4 solution (The insets show the corresponding equivalent circuit and the enlarged Nyquist plots in high-frequency region)

from 0.5 to 10 A g^{-1}. Figure 5d shows the rate capability performance of IC-MoS_2 and IE-MoS_2 at different current densities. During initial 500 cycles at 1 A g^{-1}, the stable specific capacitance was 81 F g^{-1} for IC-MoS_2 and 154 F g^{-1} for IE-MoS_2. During the following 501–1000th cycles at 2 A g^{-1}, 1001–1500th at 3 A g^{-1}, 1501–2000th at 5 A g^{-1}, and 2001–2500th at 10 A g^{-1}, the capacitance gradually decreased and still kept at a stable level. The capacitance of IE-MoS_2 achieved 166 F g^{-1} during 2501–3000th cycles at 1 A g^{-1}.

EIS measurements were conducted to investigate the charge transfer and ion diffusion properties of active electrode materials. Figure 6 shows EIS Nyquist plots of IC-MoS_2 and IE-MoS_2 in 1 M H_2SO_4 solution at the frequency range of 10^{-2}~10^5 Hz. The insets show the corresponding equivalent circuit and the enlarged Nyquist plots in the high frequency region. The elements in the equivalent circuit included the ohmic resistance (R_o), charge transfer resistance (R_{ct}), constant phase element (CPE), and Warburg element (W_o). Table 1 lists the corresponding fitting values of the equivalent circuit elements. The electrochemical complex impedance is mainly dependent on the charge transfer resistance at high frequency region and Warburg impedance at a low-frequency region. The R_o is related to the ionic resistance of electrolyte, intrinsic resistance of active materials, and the contact resistance at the active materials/current collector interface and active materials/active materials interface (Xie and Zhu 2017). The R_o value can be determined by the intercept of the arc with the real axis. The similar R_o value is determined to be 0.569 Ω for IC-MoS_2 and 0.589 Ω for IE-MoS_2. The R_{ct} is related to the charge transfer resistance at the electrode/solution interface, which is determined by high-frequency arc. Obviously, the R_{ct} value decreased from 42.43 Ω for IC-MoS_2 to 35.47 Ω for IE-MoS_2. This result indicates that IE-MoS_2 with the expanded interlayer spaces facilitates the interfacial charge transfer capability. The W_o represents diffusion impedance between the electrodes and electrolyte, which is determined by the linear slope in the low-frequency region (Iessa et al. 2016). The sloping lines of both MoS_2 samples show nearly vertical characteristic, presenting almost capacitive behavior (Aboutalebi et al. 2011). W_o is defined by W-R, W-T, and W-P. W-R is the Warburg diffusion resistance. The IE-MoS_2 shows much smaller W-R value (5.324 Ω) than IC-MoS_2 (71.11 Ω), suggesting more feasible electrolyte ion diffusion into the surface of the electrode material to conduct the electrochemical reaction. W-T is the diffusion time constant and can be estimated through the formula of $W\text{-}T = L^2/D$, where L is the effective diffusion distance of electrolyte ions and D is the effective diffusion coefficient. The IE-MoS_2 (1.281) shows much smaller W-T value than IC-MoS_2 (8.562), indicating higher ion diffusion efficiency of IE-MoS_2. W-P is the fractional exponent between 0 and 1. W-P values of IC-MoS_2 (0.467) and IE-MoS_2 (0.576) are close to 0.5, indicating Warburg impedance behavior. CPE is used to compensate for the surface non-homogeneity and surface roughness of electrode materials. CPE is defined by CPE-T and CPE-P. CPE-P is the constant phase element exponent between 0 and 1. CPE-P = 0 represents the pure

Table 1 Fitting values of equivalent circuit elements of IC-MoS_2 and IE-MoS_2 electrodes

Electrode material	R_o (Ω)	R_{ct} (Ω)	CPE		W_o		
			CPE-T	CPE-P	W-R (Ω)	W-T	W-P
IC-MoS_2	0.569	42.43	0.030	0.510	71.11	8.562	0.467
IE-MoS_2	0.589	35.47	0.073	0.747	5.324	1.281	0.576

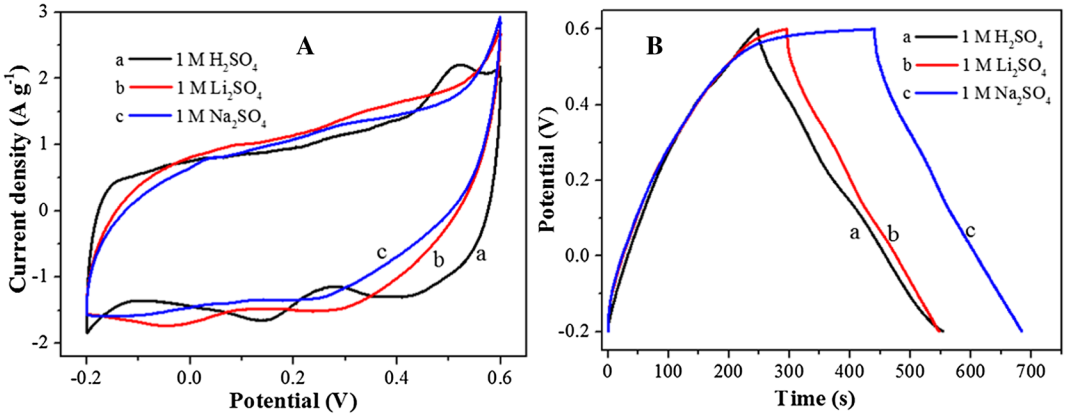

Fig. 7 **a** CV curves at 5 mV s^{-1} and **b** GCD curves at 0.5 A g^{-1} for IE-MoS_2 electrode in 1 M H_2SO_4, 1 M Li_2SO_4, and 1 M Na_2SO_4 electrolyte solution

resistor. CPE-P = 1 represents the ideal capacitor. Herein, the IE-MoS_2 (0.747) shows higher CPE-P value than IC-MoS_2 (0.510), presenting the moderate capacitor behavior of IE-MoS_2. CPE-T value is related to the capacitance of electrode materials. The IE-MoS_2 (0.073) shows higher CPE-T value than IC-MoS_2 (0.030), indicating its superior capacitive performance. The corresponding CV and GCD measurement results also prove the higher electrochemical performance of IE-MoS_2 electrode material rather than IC-MoS_2. All above analysis results prove that IE-MoS_2 is more suitable to act as a promising electrode material of supercapacitor.

Figure 7 shows CV curves at 5 mV s^{-1} and GCD curves at 0.5 A g^{-1} of IE-MoS_2 electrode in different electrolyte solution. The CV curves of IE-MoS_2 shows well-defined couple of redox peaks in H_2SO_4 electrolyte solution at a low scan rate. Comparatively, the redox peaks became insignificant in 1 M Li_2SO_4 and 1 M Na_2SO_4 electrolyte solution. It is believed that H^+ become more feasible rather than Li^+ and Na^+ to conduct ion insertion and desertion process, leading to reversible redox reaction. The response current in Li_2SO_4 electrolyte is higher than that in Na_2SO_4 electrolyte. It suggests that interlayer ion diffusion of Li^+ is more effective than that of Na^+ (Acerce et al. 2015). The GCD curves of IE-MoS2 exhibited that IR drop increased gradually when the electrolyte solution changed from H_2SO_4 to Li_2SO_4 and Na_2SO_4. The corresponding capacitance was listed in Table 2. IE-MoS_2 electrode shows much higher capacitance in H_2SO_4 than that in Li_2SO_4 and Na_2SO_4. The similar capacitance performance was achieved in Li_2SO_4 and Na_2SO_4 electrolyte solution. The ionic radius of cation increased from H^+ to Li^+ and Na^+. The delayed ion diffusion of Li^+ and Na^+ in the interlayer space of MoS_2 could affect the ion transportation, accordingly leading to the declined capacitance.

Table 2 Specific capacitance of IE-MoS_2 electrode at 0.5 A g^{-1} in 1 M H_2SO_4, 1 M Li_2SO_4, and 1 M Na_2SO_4 electrolyte solution

Electrolyte	1 M H_2SO_4	1 M Li_2SO_4	1 M Na_2SO_4
Capacitance (F g^{-1})	192	158	152

The redox process of IE-MoS_2 electrode is related with the atoms located at the surface exposed layers and at the edges (Mahmood et al. 2016; Soon and Loh 2007; Temel et al. 2010). Sulfur atoms, located on the edges and the surfaces of MoS_2, can reversibly attach protons in H_2SO_4 electrolyte. The adsorption of protons on IE-MoS_2 layers promotes accessibility of the active sulfur

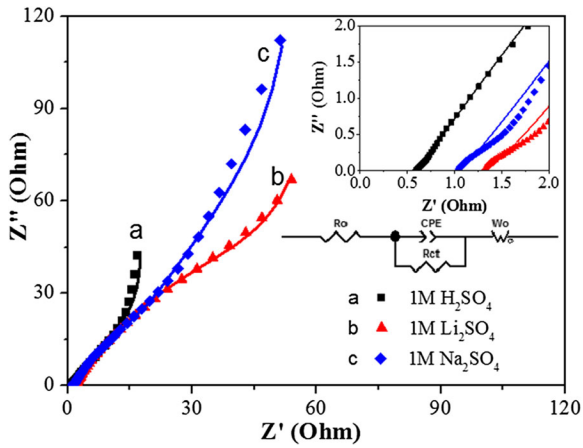

Fig. 8 EIS Nyquist plots of IE-MoS_2 in different electrolyte solution (The insets show the corresponding equivalent circuit and the enlarged Nyquist plots at high-frequency region)

Table 3 Fitting values of equivalent circuit elements of IE-MoS_2 electrode in different electrolyte solution

Electrolyte	R_o (Ω)	R_{ct} (Ω)	CPE		W_o		
			CPE-T	CPE-P	W-R (Ω)	W-T	W-P
1 M H_2SO_4	0.589	35.47	0.073	0.747	5.324	1.281	0.576
1 M Li_2SO_4	1.333	57.15	0.042	0.873	17.27	2.640	0.501
1 M Na_2SO_4	1.064	102.7	0.045	0.772	28.70	3.777	0.569

atoms. The oxidation state of the neighboring Mo atoms is changed from 4+ to (4 − δ)+ according to the reaction ($MoS_2 + H^+ + e^- \rightarrow$ MoS–SH) (Koroteev et al. 2016). Considering the high redox potential of Li^+ in MoS_2 (usually lithium insertion potential at 1.0 V), lithium ion insertion and desertion reaction ($MoS_2 + \delta Li^+ + \delta e^- \rightarrow Li_\delta MoS_2$) is unlikely to occur in aqueous solution at the low potential range from − 0.2 to 0.6 V (Yu et al. 2017).

Figure 8 shows EIS Nyquist plots of IE-MoS_2 in different electrolyte solution. The insets show the corresponding equivalent circuit and the enlarged Nyquist plots in the high-frequency region. The fitting values of the equivalent circuit elements of IE-MoS_2 are listed in Table 3. The R_o value is 0.589, 1.333, and 1.064 Ω for H_2SO_4, Li_2SO_4, and Na_2SO_4 electrolyte solution, respectively. H_2SO_4 electrolyte as a typical proton acid shows much lower ohm resistance than Li_2SO_4 and Na_2SO_4 electrolyte. The R_{ct} value of H_2SO_4 (35.47 Ω) is much smaller than that of Li_2SO_4 (57.15 Ω) and Na_2SO_4 (102.70 Ω) electrolyte, indicating more effective interfacial charge transfer capability of proton acid. The W-R value of H_2SO_4 (5.324 Ω) is much smaller than that of Li_2SO_4 (17.27 Ω) and Na_2SO_4 (28.70 Ω) electrolyte, presenting its lower Warburg diffusion resistance. The W-T value of H_2SO_4 (1.281) is much smaller than in Li_2SO_4 (2.640) and Na_2SO_4 (3.777) electrolyte, indicating higher diffusion coefficient of H_2SO_4 electrolyte. All the CPE-P values are larger than 0.5, indicating moderate capacitor behavior in three kinds of electrolyte solution. The CPE-T value in H_2SO_4 (0.073) is larger than that in Li_2SO_4 (0.042) and Na_2SO_4 (0.045), suggesting higher capacitance in H_2SO_4 rather than Li_2SO_4 and Na_2SO_4 electrolyte. This result is in accordance with the CV and GCD measurement results. In comparison with Li^+ and Na^+ ions, the proton with the smallest ion size becomes much more effective to diffuse into multilayered IE-MoS_2 through proton attachment reaction of −SH. So, IE-MoS_2 electrode possesses the superior electrochemical performance in H_2SO_4 electrolyte solution.

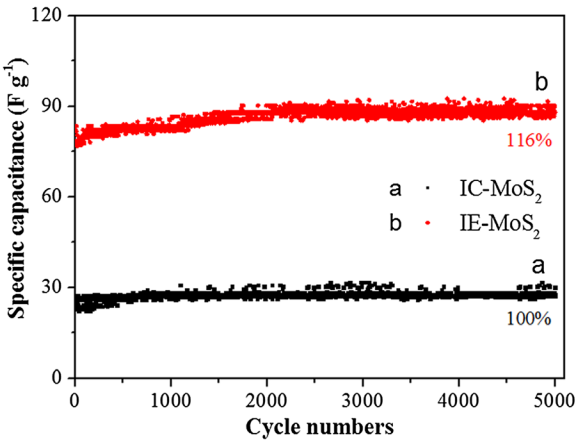

Fig. 9 Cycling stability performance of IC-MoS_2 and IE-MoS_2 at 10 A g^{-1} for 5000 cycles

Figure 9 shows the cycling performance of IC-MoS_2 and IE-MoS_2 electrode materials at 10 A g^{-1} for 5000 cycles. The continuous GCD measurement was conducted at 10 A g^{-1} from − 0.2 V to 0.6 V. IE-MoS_2 kept the good cycling stability at low capacity level of 26.1 F g^{-1}. Comparatively, IE-MoS_2 showed the increased capacitance from 76.6 to 88.8 F g^{-1}, presenting the capacity retention of 116% after 5000 cycles. The slightly increased capacity is ascribed to the electroactivation of the expanded few-layer spaces of IE-MoS_2 during the charge and discharge process, accordingly promote interface electrochemical reaction. It was also reported that the d-spacing of MoS_2 electrode material could be well expanded from 0.69 to 0. 75 nm even after charge-discharge for 50 cycles (Sahu and Mitra 2015). More accessible active sites could further contribute to improving the capacitance performance of MoS_2. So, the IE-MoS revealed the high cycling stability at high-capacity level. Table 4 lists the comparison of the electrochemical properties of IE-MoS_2 and as-reported MoS_2 electrode materials. These nanostructured MoS_2 electrode materials showed relatively high

Table 4 Comparison of electrochemical properties of IE-MoS_2 and as-reported MoS_2 electrode materials

MoS_2 electrode	Electrolyte	Specific capacitance	Cycle numbers	Capacity retention	Ref.
MoS_2 nanosheet	1.0 M Na_2SO_4	150 F g^{-1} at 1 A g^{-1}	500	22.3% at 1 A g^{-1}	Huang et al. 2014
MoS_2 nanosphere	0.5 M Na_2SO_4	145 F g^{-1} at 0.5 A g^{-1}	2000	90% at 1 A g^{-1}	Wu et al. 2016
MoS_2 nanoflower	1 M KCl	168 F g^{-1} at 1 A g^{-1}	3000	92.6% at 1 A g^{-1}	Wang et al. 2014
MoS_2 nanosheet	1 M Na_2SO_4	134 F g^{-1} at 1 A g^{-1}	1000	67.1% at 1 A g^{-1}	Zhang et al. 2017b
IE-MoS_2	1 M H_2SO_4	88.8 F g^{-1} at 10 A g^{-1}	5000	110% at 10 A g^{-1}	This work

capacity (134~168 F g^{-1}) at low current density (0.5~1.0 A g^{-1}) (Huang et al. 2014; Wang et al. 2014; Wu et al. 2016; Zhang et al. 2017b). Usually, the capacity could obviously decrease at high current density (such as 26.1 F g^{-1} at 10 A g^{-1}). However, the IE-MoS in this study achieved 88.8 F g^{-1} even at 10 A g^{-1}. Additionally, the microstructure could affect the cycling performance of MoS_2 electrode materials. These nanostructured MoS_2 showed the cycling stability with a wide variation range. Significantly, IE-MoS_2 revealed the improved capacity retention at 10 A g^{-1} even after 5000 cycles. So, IE-MoS_2 electrode material shows superior the electrochemical stability at high current density.

Electrochemical performance of IE-MoS_2 supercapacitor

Figure 10 shows CV curves at different scan rates, GCD curves at different current densities, corresponding

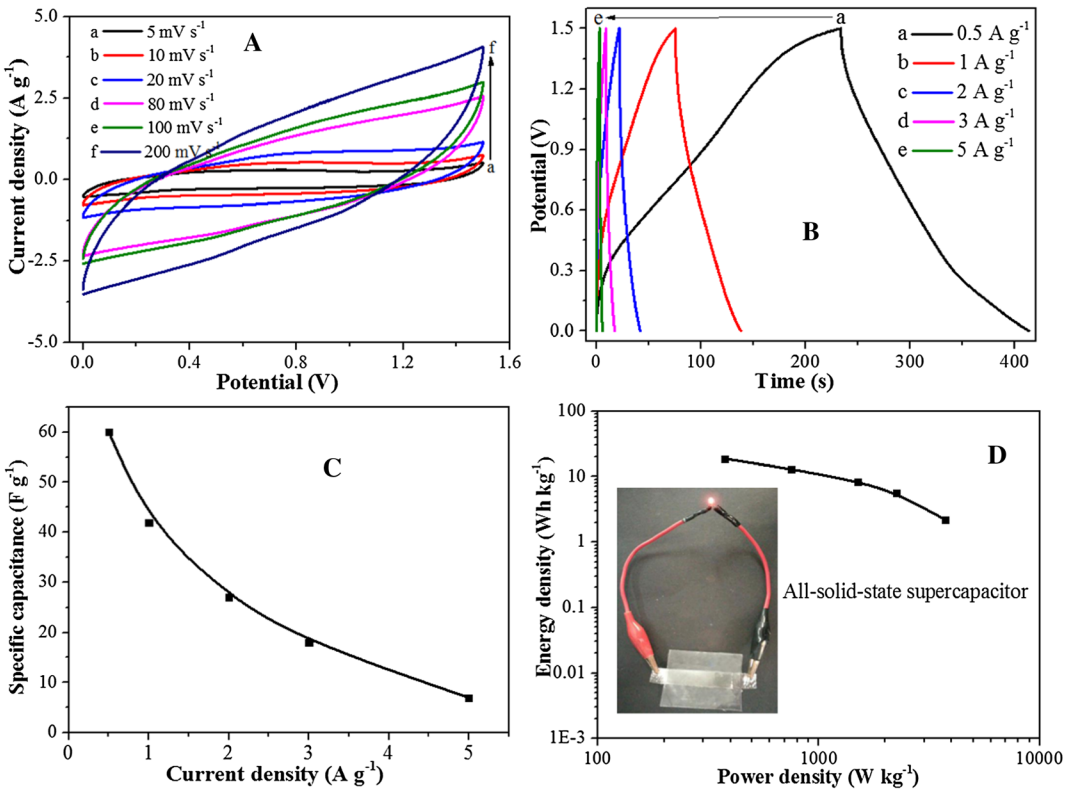

Fig. 10 Electrochemical performance of all-solid-state IE-MoS_2 supercapacitor using H_2SO_4-PVA polymer gel electrolyte. **a** CV curves at the scan rates of 5–200 mV s^{-1} and window voltage of 1.5 V. **b** GCD curves at current densities of 0.5–5.0 A g^{-1} and window voltage of 1.5 V. **c** Corresponding capacity decay curve. **d** Ragone plot (The inset shows photograph of IE-MoS_2 supercapacitor powering an LED)

capacity decay curve, and Ragone plot of all-solid-state IE-MoS_2 supercapacitor. The corresponding specific capacitance (C), energy density (E), and power density (P) are calculated using equation 1, 2 and 3, respectively. Figure 10a shows CV curve of all-solid-state IE-MoS_2 supercapacitor using H_2SO_4-PVA polymer gel electrolyte at a scan rate of 5 mV s^{-1} and window voltage of 1.5 V. IE-MoS_2 supercapacitor using H_2SO_4-PVA polymer gel electrolyte does not show obvious redox peak at positive window voltage. Concerning the highly delayed ion diffusion of solid-state electrolyte, hydrogen ion intercalation into MoS_2 interlayer becomes insufficient in H_2SO_4-PVA polymer gel electrolyte, causing the restrained hydrogen reduction process. The proton insertion/desertion into MoS_2 becomes insignificant Faradaic process. The adsorption of proton on the surface of MoS_2 results in the nonFaradaic process ((MoS_2) surface $+ H^+ + e^- \rightarrow$ (MoS_2-H) surface). Figure 10b, c show that the specific capacitance of IE-MoS_2 supercapacitor was 60 F g^{-1} at 0.5 A g^{-1}. Figure 10d shows that the energy density decreased from 18.75 to 2.19 Wh kg^{-1} at high window voltage of 1.5 V when the power density increased from 375 to 3750 W kg^{-1}. The inset in Fig. 10d shows photograph of IE-MoS_2 supercapacitor powering an LED light. Thus, all-solid-state IE-MoS_2 supercapacitor had good electrochemical energy storage performance, presenting a promising energy storage application.

The cycling performance was measured for IE-MoS_2 supercapacitor using H_2SO_4-PVA gel electrolyte. Figure 11 shows the capacity retention of all-solid-state IE-MoS_2 supercapacitor at 1 A g^{-1}. The cycling performance is measured by LAND CT2001A battery testing system. But the capacitance performance via GCD curves is measured by CHI760C electrochemical workstation. So, the measured capacitance results may have a little difference. Continuous GCD measurement was conducted at 1 A g^{-1} and the window voltage of 1.5 V. The specific capacitance increased from 50.08 to 55.12 F g^{-1}. The capacity retention even achieved about 110% after 1000 cycles. As-reported MoS_2 supercapacitor only showed the energy density of 5.42 Wh kg^{-1} at 0.8 mA g^{-1} (Javed et al. 2015). Graphene-MoS_2 supercapacitor showed the increased energy density of 24.59 Wh kg^{-1} at 6.5 mA g^{-1} (Javed et al. 2015). The reasonable cycling stability was achieved to keep the capacity retention above 90% after 1400 cycles. Comparatively, all-solid-state IE-MoS_2 supercapacitor could keep both high energy density (18.75 Wh kg^{-1}) and cycling stability (even above 100%) as well. So, IE-MoS_2 electrode material still had good electrochemical energy storage performance and presented a promising energy storage application.

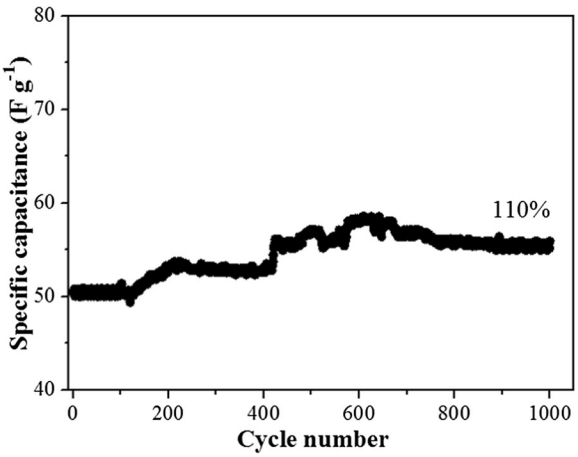

Fig. 11 Capacity retention curve of all-solid-state IE-MoS_2 supercapacitor at 1 A g^{-1}

Conclusions

The interspace-expanded MoS_2 few-layer was prepared through hydrothermal synthesis and then ultrasound exfoliation process. The specific capacitance of IE-MoS_2 electrode was 192 F g^{-1} at 0.5 A g^{-1} in 1.0 M H_2SO_4 electrolyte solution. The capacity retention was 42% when the current density increased from 0.5 to 5 A g^{-1}. The overall capacity retention was 116% after 5000 charge-discharge cycles in H_2SO_4 electrolyte solution, presenting good cycling performance. Superior specific capacitance and cycling performance were ascribed to the expanded interlayer spaces of IE-MoS_2. The improved capacity retention even above 100% was ascribed to the electro-activation of the expanded few-layer in H_2SO_4 electrolyte solution. All-solid-state IE-MoS_2 supercapacitor based on H_2SO_4-PVA gel electrolyte were determined to be energy density of 18.75 Wh kg^{-1} and power density of 375 W kg^{-1} at 0.5 A g^{-1} and window voltage of 1.5 V. The overall capacity retention was 110% after 1000 charge-discharge cycles, presenting good electrochemical stability. IE-MoS_2 could be well used as all-solid-state supercapacitor electroactive material, exhibiting the promising energy storage application.

Acknowledgements The work was supported by National Natural Science Foundation of China (No. 21373047), Graduate Innovation Program of Jiangsu Province, the Fundamental Research Funds for the Central Universities (2242018K41024) and the Priority Academic Program Development of Jiangsu Higher Education Institutions.

Compliance with ethical standards

Conflict of interest The authors declare that they have no conflict of interest.

References

Aboutalebi SH, Chidembo AT, Salari M, Konstantinov K, Wexler D, Liu HK, Dou SX (2011) Comparison of GO, GO/MWCNTs composite and MWCNTs as potential electrode materials for supercapacitors. Energy Environ Sci 4:1855. https://doi.org/10.1039/c1ee01039e

Acerce M, Voiry D, Chhowalla M (2015) Metallic 1T phase MoS_2 nanosheets as supercapacitor electrode materials. Nat Nanotechnol 10:313–318. https://doi.org/10.1038/nnano.2015.40

Bissett MA, Kinloch IA, Dryfe RAW (2015) Characterization of MoS2-graphene composites for high-performance coin cell supercapacitors. ACS Appl Mater Interface 7:17388–17398. https://doi.org/10.1021/acsami.5b04672

Cunningham G, Lotya M, Cucinotta CS, Sanvito S, Bergin SD, Menzel R, Shaffer MSP, Coleman JN (2012) Solvent exfoliation of transition metal dichalcogenides: dispersibility of exfoliated nanosheets varies only weakly between compounds. ACS Nano 6:3468–3480. https://doi.org/10.1021/nn300503e

Du G, Guo Z, Wang S, Zeng R, Chen Z, Liu H (2010) Superior stability and high capacity of restacked molybdenum disulfide as anode material for lithium ion batteries. Chem Commun 46:1106–1108. https://doi.org/10.1039/b920277c

Fei L, Xu Y, Wu X, Chen G, Li Y, Li B, Deng S, Smirnov S, Fan H, Luo H (2014) Instant gelation synthesis of 3D porous MoS_2@C nanocomposites for lithium ion batteries. Nanoscale 6:3664–3669. https://doi.org/10.1039/c3nr05815h

Ghasemi F, Mohajerzadeh S (2016) Sequential solvent exchange method for controlled exfoliation of MoS2 suitable for phototransistor fabrication. ACS Appl Mater Interface 8:31179–31191. https://doi.org/10.1021/acsami.6b07211

Hu Z, Wang L, Zhang K, Wang J, Cheng F, Tao Z, Chen J (2014) MoS2 Nanoflowers with expanded interlayers as high-performance anodes for sodium-ion batteries. Angew Chem 53:12794–12798

Huang K-J, Wang L, Zhang J-Z, Wang L-L, Mo Y-P (2014) One-step preparation of layered molybdenum disulfide/multi-walled carbon nanotube composites for enhanced performance supercapacitor. Energy 67:234–240. https://doi.org/10.1016/j.energy.2013.12.051

Iessa KHS, Zhang Y, Zhang G, Xiao F, Wang S (2016) Conductive porous sponge-like ionic liquid-graphene assembly decorated with nanosized polyaniline as active electrode material for supercapacitor. J Power Sources 302:92–97. https://doi.org/10.1016/j.jpowsour.2015.10.036

Javed MS, Dai S, Wang M, Guo D, Chen L, Wang X, Hu C, Xi Y (2015) High performance solid state flexible supercapacitor based on molybdenum sulfide hierarchical nanospheres. J Power Sources 285:63–69. https://doi.org/10.1016/j.jpowsour.2015.03.079

Jeong S, Shin HY, Shin RH, Jo W, Yoon S, Rubhausen M (2015) Raman scattering studies of the lattice dynamics in layered MoS2. J Korean Phys Soc 66:1575–1580. https://doi.org/10.3938/jkps.66.1575

Koroteev VO, Kuznetsova IV, Kurenya AG, Kanygin MA, Fedorovskaya EO, Mikhlin YL, Chuvilin AL, Bulusheva LG, Okotrub AV (2016) Enhanced supercapacitance of vertically aligned multi-wall carbon nanotube array covered by MoS2nanoparticles. Phys Status Solidi B 253:2451–2456. https://doi.org/10.1002/pssb.201600366

Lee Y-H, Zhang XQ, Zhang W, Chang MT, Lin CT, Chang KD, Yu YC, Wang JTW, Chang CS, Li LJ, Lin TW (2012) Synthesis of large-area MoS2 atomic layers with chemical vapor deposition. Adv Mater 24:2320–2325. https://doi.org/10.1002/adma.201104798

Liu H, Su D, Zhou R, Sun B, Wang G, Qiao SZ (2012) Highly ordered mesoporous MoS2 with expanded spacing of the (002) crystal plane for ultrafast lithium ion storage. Adv Energy Mater 2:970–975

Liu W, Zhao C, Zhou R, Zhou D, Liu Z, Lu X (2015) Lignin-assisted exfoliation of molybdenum disulfide in aqueous media and its application in lithium ion batteries. Nanoscale 7:9919–9926. https://doi.org/10.1039/c5nr01891a

Liu AP, Zhao L, Zhang JM, Lin LX, Wu HP (2016) Solvent-assisted oxygen incorporation of vertically aligned MoS2 ultrathin nanosheets decorated on reduced graphene oxide for improved electrocatalytic hydrogen evolution. ACS Appl Mater Interface 8:25210–25218. https://doi.org/10.1021/acsami.6b06031

Lu L, Xie Y (2017) Fabrication and supercapacitor behavior of phosphomolybdic acid/polyaniline/titanium nitride core-shell nanowire array. New J Chem 41:335–346. https://doi.org/10.1039/c6nj02368a

Lu Y, Yao X, Yin J, Peng G, Cui P, Xu X (2015) MoS2 nanoflowers consisting of nanosheets with a controllable interlayer distance as high-performance lithium ion battery anodes. RSC Adv 5:7938–7943

Lu L, Xie Y, Zhao Z (2018) Improved electrochemical stability of NixCo2x(OH)(6x)/NiCo2O4 electrode material. J Alloys Compd 731:903–913. https://doi.org/10.1016/j.jallcom.2017.10.119

Mahmood Q, Park SK, Kwon KD, Chang SJ, Hong JY, Shen G, Jung YM, Park TJ, Khang SW, Kim WS, Kong J, Park HS (2016) Transition from diffusion-controlled intercalation into extrinsically pseudocapacitive charge storage of MoS2 by nanoscale heterostructuring. Adv Energy Mater 6. https://doi.org/10.1002/aenm.201501115

Matte HSSR, Gomathi A, Manna AK, Late DJ, Datta R, Pati SK, Rao CNR (2010) MoS2 and WS2 analogues of graphene. Angew Chem Int Ed 49:4059–4062. https://doi.org/10.1002/anie.201000009

Nagaraju G, Tharamani CN, Chandrappa GT, Livage J (2007) Hydrothermal synthesis of amorphous MoS2 nanofiber bundles via acidification of ammonium heptamolybdate tetrahydrate. Nanoscale Res Lett 2:461–468. https://doi.org/10.1007/s11671-007-9087-z

Park MH, Noh M, Lee S, Ko M, Chae S, Sim S, Choi S, Kim H, Nam H, Park S, Cho J (2014) Flexible high-energy li-ion batteries with fast-charging capability. Nano Lett 14:4083–4089. https://doi.org/10.1021/nl501597s

Patel R, Inamdar AI, Kim HB, Im H, Kim H (2016) In-situ hydrothermal synthesis of a MoS2 nanosheet electrode for electrochemical energy storage applications. J Korean Phys Soc 68:1341–1346. https://doi.org/10.3938/jkps.68.1341

Sahu TS, Mitra S (2015) Exfoliated MoS2 sheets and reduced graphene oxide—an excellent and fast anode for sodium-ion battery. Sci Rep 5:12571–12571

Soon JM, Loh KP (2007) Electrochemical double-layer capacitance of MoS2 nanowall films. Electrochem Solid-State Lett 10:A250–A254. https://doi.org/10.1149/1.2778851

Tang H, Wang J, Yin H, Zhao H, Wang D, Tang Z (2015) Growth of polypyrrole ultrathin films on MoS2 monolayers as high-performance supercapacitor electrodes. Adv Mater 27:1117–1123. https://doi.org/10.1002/adma.201404622

Temel B, Tuxen AK, Kibsgaard J, Topsøe NY, Hinnemann B, Knudsen KG, Topsøe H, Lauritsen JV, Besenbacher F (2010) Atomic-scale insight into the origin of pyridine inhibition of MoS2-based hydrotreating catalysts. J Catal 271:280–289. https://doi.org/10.1016/j.jcat.2010.02.007

Wang X, Ding J, Yao S, Wu X, Feng Q, Wang Z, Geng B (2014) High supercapacitor and adsorption behaviors of flower-like MoS2nanostructures. J Mater Chem A 2:15958–15963. https://doi.org/10.1039/c4ta03044c

Wang J, Wu Z, Hu K, Chen X, Yin H (2015) High conductivity graphene-like MoS2/polyaniline nanocomposites and its application in supercapacitor. J Alloys Compd 619:38–43. https://doi.org/10.1016/j.jallcom.2014.09.008

Wang K, Li L, Liu Y, Zhang C, Liu T (2016) Constructing a "pizza-like" MoS2/Polypyrrole/polyaniline ternary architecture with high energy density and superior cycling stability for supercapacitors. Adv Mater Interfaces 3:1600665. https://doi.org/10.1002/admi.201600665

Wang H, Jiang H, Hu Y, Li N, Zhao X, Li C (2017a) 2D MoS2/polyaniline heterostructures with enlarged interlayer spacing for superior lithium and sodium storage. J Mater Chem A 5:5383–5389. https://doi.org/10.1039/c7ta00030h

Wang T, Chen S, Pang H, Xue H, Yu Y (2017b) MoS_2-based nanocomposites for electrochemical energy storage. Adv Sci (Weinh) 4:1600289–1600289. https://doi.org/10.1002/advs.201600289

Wu JZ, Dai J, Shao YB, Cao MQ, Wu XH (2016) Carbon dot-assisted hydrothermal synthesis of flower-like MoS2 nanospheres constructed by few-layered multiphase MoS2 nanosheets for supercapacitors. RSC Adv 6:77999–78007. https://doi.org/10.1039/c6ra15074h

Xiao H, Wang S, Zhang S, Wang Y, Xu Q, Hu W, Zhou Y, Wang Z, An C, Zhang J (2017) Interlayer expanded molybdenum disulfide nanosheets assembly for electrochemical supercapacitor with enhanced performance. Mater Chem Phys 192:100–107. https://doi.org/10.1016/j.matchemphys.2017.01.077

Xie Y (2017) Overview of supercapacitance performance of graphene supported on porous substrates. Mater Tech 32:355–366. https://doi.org/10.1080/10667857.2016.1242198

Xie Y, Gao R (2017) Electrochemical capacitance of titanium nitride modified lithium titanate nanotube array. J Alloys Compd 725:1–13. https://doi.org/10.1016/j.jallcom.2017.05.179

Xie Y, Sha X (2018) Electrochemical cycling stability of nickel (II) coordinated polyaniline. Synth Met 237:29–39. https://doi.org/10.1016/j.synthmet.2018.01.011

Xie Y, Tian F (2017) Capacitive performance of molybdenum nitride/titanium nitride nanotube array for supercapacitor. Mater Sci Eng B 215:64–70. https://doi.org/10.1016/j.mseb.2016.11.005

Xie Y, Wang J (2018) Capacitance performance of carbon paper supercapacitor using redox-mediated gel polymer electrolyte. J Sol-Gel Sci Technol 86:760–772

Xie Y, Zhu F (2017) Electrochemical capacitance performance of polyaniline/tin oxide nanorod array for supercapacitor. J Solid State Electrochem 21:1675–1685. https://doi.org/10.1007/s10008-017-3525-3

Xiong F, Cai Z, Qu L, Zhang P, Yuan Z, Asare OK, Xu W, Lin C, Mai L (2015) Three-dimensional crumpled reduced graphene oxide/MoS_2 nanoflowers: a stable anode for lithium-ion batteries. ACS Appl Mater Interface 7:12625–12630. https://doi.org/10.1021/acsami.5b02978

Yoo HD, Li YF, Liang YL, Lan YC, Wang F, Yao Y (2016) Intercalation pseudocapacitance of exfoliated molybdenum disulfide for ultrafast energy storage. Chemnanomat 2:688–691. https://doi.org/10.1002/cnma.201600117

Yu X-Y, Yu L, Lou XWD (2017) Hollow nanostructures of molybdenum sulfides for electrochemical energy storage and conversion. Small Methods 1:1600020. https://doi.org/10.1002/smtd.201600020

Zhang Y, Sun W, Rui X, Li B, Tan HT, Guo G, Madhavi S, Zong Y, Yan Q (2015) One-pot synthesis of tunable crystalline Ni3 S4 @amorphous MoS2 Core/Shell Nanospheres for high-performance Supercapacitors. Small 11:3694–3702. https://doi.org/10.1002/smll.201403772

Zhang P, Qin F, Zou L, Wang M, Zhang K, Lai Y, Li J (2017a) Few-layered MoS2/C with expanding d-spacing as a high-performance anode for sodium-ion batteries. Nanoscale

Zhang S, Hu R, Dai P, Yu X, Ding Z, Wu M, Li G, Ma Y, Tu C (2017b) Synthesis of rambutan-like MoS2/mesoporous carbon spheres nanocomposites with excellent performance for supercapacitors. Appl Surf Sci 396:994–999. https://doi.org/10.1016/j.apsusc.2016.11.074

Zhao Z, Xie Y (2017) Enhanced electrochemical performance of carbon quantum dots-polyaniline hybrid. J Power Sources 337:54–64. https://doi.org/10.1016/j.jpowsour.2016.10.110

Zhou Y, Xie Y (2017) Capacitive performance of ruthenium-coordinated polypyrrole. New J Chem 41:10312–10323. https://doi.org/10.1039/c7nj01151b